

SOLVING ATOMIC STRUCTURE USING STATISTICAL MECHANICAL SEARCHES ON  
X-RAY SCATTERING DERIVED POTENTIAL ENERGY SURFACES

by

Christopher James Wright

Bachelor of Science  
Brown University 2014

---

Submitted in Partial Fulfillment of the Requirements

for the Degree of Masters of Science in

Chemical Engineering

College of Engineering and Computing

University of South Carolina

2016

Accepted by:

Xiao-Dong Zhou, Major Professor

Thomas Vogt, Committee Member

Mark Uline, Committee Member

Jochen Lauterbach, Committee Member

Lacy Ford, Vice Provost and Dean of Graduate Studies

© Copyright by Christopher James Wright, 2016  
All Rights Reserved.

## DEDICATION

## ACKNOWLEDGMENTS

## ABSTRACT

## TABLE OF CONTENTS

DEDICATION . . . . .	iii
ACKNOWLEDGMENTS . . . . .	iv
ABSTRACT . . . . .	v
LIST OF TABLES . . . . .	ix
LIST OF FIGURES . . . . .	x
TODO LIST . . . . .	1
CHAPTER 1 ATOMIC STRUCTURE: EXTRACTION AND APPLICATION . . .	3
1.1 Atomistic Goals . . . . .	3
1.2 Atomistic Experiments . . . . .	4
1.3 Atomistic Simulations . . . . .	4
CHAPTER 2 STATISTICAL MECHANICAL ENSEMBLES AND POTENTIAL ENERGY SURFACES . . . . .	5
2.1 Introduction . . . . .	5
2.2 Potential Energy Surfaces . . . . .	5
2.3 Ensembles . . . . .	7

<b>CHAPTER 3 ATOMIC PAIR DISTRIBUTION FUNCTION: THEORY AND COMPUTATION . . . . .</b>	<b>12</b>
3.1 Theory . . . . .	12
3.2 Computation . . . . .	14
3.3 Experiment . . . . .	17
3.4 Data Processing Workflow . . . . .	18
<b>CHAPTER 4 BENCHMARKING . . . . .</b>	<b>33</b>
4.1 PDF . . . . .	33
4.2 PDF with ADPs . . . . .	33
<b>CHAPTER 5 ANNEALING AND AGGREGATION OF 2NM AU NANOPARTICLES . . . . .</b>	<b>34</b>
5.1 Experiments . . . . .	34
5.2 Data Processing . . . . .	34
5.3 Data Analysis . . . . .	34
5.4 Simulation . . . . .	34
5.5 Structural Analysis . . . . .	34
5.6 Conclusions . . . . .	34
<b>CHAPTER 6 PHASE CHANGES AND ANNEALING DYNAMICS OF <math>\text{Pr}_2\text{NiO}_4</math> AND ITS DERIVATIVES . . . . .</b>	<b>35</b>
6.1 Experiments . . . . .	35
6.2 Data Processing . . . . .	35
6.3 Data Analysis . . . . .	35
6.4 Simulation . . . . .	35

6.5	Structural Analysis . . . . .	35
6.6	Conclusions . . . . .	35
CHAPTER 7	CONCLUSION . . . . .	36

## LIST OF TABLES

## LIST OF FIGURES

Figure 3.1 Comparison of the CPU and GPU chip architectures . . . . .	15
Figure 3.2 Database Loading Workflow. Data is loaded from various sources, including images and text files, into the FileStore and Meta-dataStore databases. Data is then retrieved from the databases using the databroker. . . . .	18
Figure 3.3 Scattering onto a flat detector . . . . .	19
Figure 3.4 $Q$ resolution as a function of $Q$ . . . . .	20
Figure 3.5 Number of pixels as a function of $Q$ , binned at the $Q$ resolution of the detector. . . . .	21
Figure 3.6 Generated dead/hot pixel masks for a detector with 100 bad pixels. a) the standard even bin mask and b) the $Q$ resolution binned mask . . . . .	23
Figure 3.7 Generated dead/hot pixel masks for a detector with 300 bad pixels. a) the standard even bin mask and b) the $Q$ resolution binned mask . . . . .	23
Figure 3.8 Generated dead/hot pixel masks for a detector with 500 bad pixels. a) the standard even bin mask and b) the $Q$ resolution binned mask . . . . .	24
Figure 3.9 Generated dead/hot pixel masks for a detector with 1000 bad pixels. a) the standard even bin mask and b) the $Q$ resolution binned mask . . . . .	24
Figure 3.10 Generated beamstop holder masks for a beamstop holder with 10% transmittance. a) the raw image, b) the masked image, c) and the missed pixels . . . . .	25
Figure 3.11 Generated beamstop holder masks for a beamstop holder with 30% transmittance. a) the raw image, b) the masked image, c) and the missed pixels . . . . .	25

Figure 3.12 Generated beamstop holder masks for a beamstop holder with 50% transmittance. a) the raw image, b) the masked image, c) and the missed pixels . . . . .	25
Figure 3.13 Generated beamstop holder masks for a beamstop holder with 90% transmittance. a) the raw image, b) the masked image, c) and the missed pixels . . . . .	26
Figure 3.14 Generated beamstop holder masks which is rotated away from verticle . . . . .	26
Figure 3.15 Masked experimental data. a) the raw image, b) the mask . . . . .	27
Figure 3.16 Masked experimental data with Pt single crystal signal. a) the raw image, b) the mask . . . . .	28
Figure 3.17 Masked experimental data with Pt single crystal signal using figure's 3.15 as a starting mask. a) the raw image, b) the mask . . . . .	28
Figure 3.18 Masking, average, and % standard deviation of an example x-ray total scattering measurement. This image was produced with no mask. a) the image, b) the mean and median values, c) % standard deviation (normalized to the median), d) a closeup of the $28 \text{ \AA}^{-1}$ to $31 \text{ \AA}^{-1}$ $Q$ range for the mean and median, e) $\text{\AA}^{-1}$ to $31 \text{ \AA}^{-1}$ $Q$ range for the standard deviation . . . . .	30
Figure 3.19 Masking, average, and % standard deviation of an example x-ray total scattering measurement. This image was produced with only an edge mask. a) the image, b) the mean and median values, c) % standard deviation (normalized to the median), d) a closeup of the $28 \text{ \AA}^{-1}$ to $31 \text{ \AA}^{-1}$ $Q$ range for the mean and median, e) $\text{\AA}^{-1}$ to $31 \text{ \AA}^{-1}$ $Q$ range for the standard deviation . . . . .	31
Figure 3.20 Masking, average, and % standard deviation of an example x-ray total scattering measurement. This image was produced combining an edge mask combined and the automatically generated mask. a) the image, b) the mean and median values, c) % standard deviation (normalized to the median), d) a closeup of the $28 \text{ \AA}^{-1}$ to $31 \text{ \AA}^{-1}$ $Q$ range for the mean and median, e) $\text{\AA}^{-1}$ to $31 \text{ \AA}^{-1}$ $Q$ range for the standard deviation . . . . .	32

1

## TODO LIST

## INTRODUCTION

3 This is the introduction to the thesis.

# CHAPTER 1

## 5 ATOMIC STRUCTURE: EXTRACTION AND APPLICATION

### 6 1.1 ATOMISTIC GOALS

7 The only way to truly understand the fundamental souce of material and chemical  
8 properties is through atomic structure. The goal of atomistic engineering is to pro-  
9 duce novel structures and combinations of structures to engender new properties and  
10 functions. This includes producing stronger materials, more durable catalysts, more  
11 energy dense batteries, and many more engineering applicatons. The true power of  
12 atomistic engineering has been shown in biochemistry and pharmicuttical design. Al-  
13 though the production of drugs and biomeical treatments is usually considered to be  
14 rather far from the field of catalyst design and materials science, the atomistic nature  
15 of these fields can not be denied. The field of protene structural analysis stands  
16 as an example of structural science, elcuidating the three dimensional coordinates of  
17 thousands of atoms. These structures are then used to describe how the molecular  
18 machinery of the biological world works, enabling the development of new drugs and  
19 treatments for diseases and a deeper understanding of how we evolved. The develop-  
20 ment of protene inhibitor drugs, which are important to so many treatments, would  
21 have not been possible without very detailed atomic structures. The asperation of  
22 this work is to create this level of accuracy and utility, generating structures which  
23 allow for the understanding of how materials work on a fundamental level.

24 **1.2 ATOMISTIC EXPERIMENTS**

25 **Single Crystal Diffraction**

26 **Electron Microscopy**

27 **X-ray Total Scattering**

28 **1.3 ATOMISTIC SIMULATIONS**

29 The goals of atomistic simulations are usually to produce atomic structures from  
30 quantum mechanical first principles, as in the case of Density Functional Theory  
31 (DFT), or classical approximations to quantum mechanics.

32 **Density Functional Theory**

33 **Classical Force Field**

34 **Monte Carlo and Statistical Mechanics**

35 Maybe put the ensemble and PES work here, since it is more general than the PDF  
36 per say. Also the rational for the gradients and fast computation make much more  
37 sense knowing we are going to be very sample happy and follow the gradient of the  
38 PES.

39

## CHAPTER 2

40

# STATISTICAL MECHANICAL ENSEMBLES AND POTENTIAL ENERGY SURFACES

42 2.1 INTRODUCTION

43 The approach taken in this work for solving the atomic structures of materials is  
44 one of optimization. The positional variables of the system are optimized so as to  
45 minimize the value of a potential energy surface (PES). The

46 2.2 POTENTIAL ENERGY SURFACES

47 A PES simply describes the potential energy of the system as a function of all its  
48 relevant coordinates in phase space, essentially providing a mapping  $\mathbb{R}^n \rightarrow \mathbb{R}$ . Usually  
49 these coordinates are the positions of the atoms  $q$  and their conjugate momenta  $p$ .  
50 Note that there could be more variables associated with the system, for instance the  
51 magnetic moments of the atoms could play a role in describing the system. In this  
52 magnetic system there would be positional variables for the atomwise spin vectors  
53 and their "momenta". Application of the term "momenta" might seem odd here, as  
54 the magnetic spin does not have a mass or a velocity. However, since the magnetic  
55 "position" is defined on the PES we need to describe its conjugate variable to properly  
56 formulate Hamiltonian dynamics and the kinetic portion of the PES.

57 **Experimentally Derived Potential Energy Surfaces**

58 Generally PESs are obtained from purely computational experiments including: ab-  
 59 initio DFT, classical approximations via the embedded atom method, or even param-  
 60 eter driven models with experimentally fitted parameters. However, one can derive  
 61 a PES from an experiment which describes how well the model reproduces the ex-  
 62 perimental data. In this case one needs a theoretical and computational framework  
 63 mapping the atomistic variables of the simulation to the same space of the data ob-  
 64 tained from the experiment. This allows the experiment to be compared directly  
 65 against the predicted data via an experimentally derived PES.

66 **Potentials**

67 For an experiment which produces 1D data, like powder diffraction, EXAFS or XPS,  
 68 the implemented potentials are:

$$\chi^2 = \sum_{a=a_{\min}}^{a_{\max}} (A_{\text{obs}} - \alpha A_{\text{calc}})^2 \quad (2.1)$$

$$Rw = \sqrt{\frac{\sum_{a=a_{\min}}^{a_{\max}} (A_{\text{obs}} - \alpha A_{\text{calc}})^2}{\sum_{a=a_{\min}}^{a_{\max}} A_{\text{obs}}^2}} \quad (2.2)$$

$$\chi_{\text{INVERT}}^2 = \frac{1}{N} \sum_j \sum_r [A_{\text{obs}}(r) - \alpha A_{j,\text{calc}}(r)]^2 \quad (2.3)$$

$$\alpha = \frac{\sum_{a=a_{\min}}^{a_{\max}} A_{\text{obs}} A_{\text{calc}}}{\sum_{a=a_{\min}}^{a_{\max}} A_{\text{calc}}^2} = \frac{\vec{A}_{\text{obs}} \cdot \vec{A}_{\text{calc}}}{|\vec{A}_{\text{calc}}|^2} \quad (2.4)$$

72 where  $A_{\text{calc}}$  and  $A_{\text{obs}}$  are the calculated and observed 1D experimental data and  $A_{\text{calc},j}$   
 73 is the calculated data for a single atom interacting with the other atoms of the system.  
 74 Note that  $A_{\text{calc}}$  has a dependence on  $q$ , the positions of the system.

75 **Forces**

$$\vec{\nabla} \chi^2 = -2 \sum_{a=a_{\min}}^{a_{\max}} (\alpha \frac{\partial A_{\text{calc}}}{\partial \gamma_{i,w}} + A_{\text{calc}} \frac{\partial \alpha}{\partial \gamma_{i,w}})(A_{\text{obs}} - \alpha A_{\text{calc}}) \quad (2.5)$$

76

$$\vec{\nabla}Rw = \frac{Rw}{\chi^2} \sum_{a=a_{\min}}^{a_{\max}} (\alpha \frac{\partial A_{\text{calc}}}{\partial \gamma_{i,w}} + A_{\text{calc}} \frac{\partial \alpha}{\partial \gamma_{i,w}})(\alpha A_{\text{calc}} - (A_{\text{obs}})) \quad (2.6)$$

77

$$\frac{\partial \alpha}{\partial \gamma_{i,w}} = \frac{(\sum_{a=a_{\min}}^{a_{\max}} A_{\text{obs}} \frac{\partial A_{\text{calc}}}{\partial \gamma_{i,w}} - 2\alpha \sum_{a=a_{\min}}^{a_{\max}} A_{\text{calc}} \frac{\partial A_{\text{calc}}}{\partial \gamma_{i,w}})}{\sum_{a=a_{\min}}^{a_{\max}} A_{\text{calc}}^2} \quad (2.7)$$

78

$$\vec{\nabla}\chi^2_{\text{INVERT}} = \frac{-2}{N} \sum_{a=a_{\min}}^{a_{\max}} \sum_j (\alpha \frac{\partial A_{j,\text{calc}}}{\partial \gamma_{i,w}} + A_{j,\text{calc}} \frac{\partial \alpha}{\partial \gamma_{i,w}})(A_{\text{obs}} - \alpha A_{j,\text{calc}}) \quad (2.8)$$

79 where  $\gamma_{i,w}$  is the  $i$ th arbitrary positional variable in the  $w$ th direction. The concept  
 80 of an "arbitrary positional variable" might seem a bit cumbersome but it allows us  
 81 to define the forces for any atomic parameter which can be represented as a vector  
 82 in 3-space. This comes in handy when trying to define the forces acting on variables  
 83 like anisotropic displacement parameters or atomic magnetic spins.

84 DISCUSS INVERT A BUNCH. ALSO COMPARE RW AND CHI\*\*2, POTEN-  
 85 TIALY WITH A FIGURE.

86 2.3 ENSEMBLES

87 While PESs describe which atomic configurations are the most desirable and how  
 88 the atoms would like to get there, the ensemble describes how the atoms move on  
 89 the PES. The abstraction of the PES from the ensemble is an important one, as it  
 90 allows for the reuse and exchange of both PESs and ensembles for a wide array of  
 91 problems. Statistical mechanical ensembles can be described in two ways, analytically  
 92 and stochastically. For long simulation times and fine enough numerical or analytical  
 93 integration these two descriptions should be identical. In either case one starts by  
 94 defining the Hamiltonian  $\mathcal{H}$  as the total energy of the system. Thus, the Hamiltonian  
 95 is described as the sum of the potential  $U(q)$  and kinetic  $K(p)$  energies, where  $q$  is  
 96 the positions of the atoms and  $p$  is their momenta

$$\mathcal{H}(q, p) = U(q) + K(p) \quad (2.9)$$

97 where  $K(p) = \frac{1}{2} \sum_i \frac{p_i^2}{m_i}$  and  $i$  denotes the  $i$ th particle. Analytically one generally defines  
 98 a partition function, which describes the sum of probabilities over all potential atomic  
 99 states.

$$\Xi = \sum_i P_i(q, p)$$

100 where  $P_i$  is the probability of the  $i$ th state and is a function of the total energy of  
 101 that state. This partition function can then be used to obtain the probability of any  
 102 specific state.

## 103 Hamiltonian Monte Carlo

In order to model dynamics we need to describe the motion of the particles in our system, thus:

$$\frac{dq_i}{dt} = \frac{\partial \mathcal{H}}{\partial p_i} = p_i \quad (2.10)$$

$$\frac{dp_i}{dt} = -\frac{\partial \mathcal{H}}{\partial q_i} = -\vec{\nabla}U \quad (2.11)$$

Using these equations we can derive the position and momentum vectors at any point in time using the leap-frog algorithm:

$$p_i(t + \delta t/2) = p_i(t) - \frac{\delta t}{2} \frac{\partial}{\partial q_i} U(q(t)) \quad (2.12)$$

$$q_i(t + \delta t) = q_i(t) + \delta t * p_i(t + \delta t/2) \quad (2.13)$$

$$p_i(t + \delta t) = p_i(t + \delta t/2) - \frac{\delta t}{2} \frac{\partial}{\partial q_i} U(q(t + \delta t)) \quad (2.14)$$

104 Note that  $\frac{\partial}{\partial q_i}$  is the gradient with respect to  $q$  where  $i$  denotes the  $i$ th atom being  
 105 moved. Using this notation the gradient is

$$\vec{\nabla}U = \begin{bmatrix} \frac{\partial U}{\partial q_{0,x}} & \frac{\partial U}{\partial q_{0,y}} & \frac{\partial U}{\partial q_{0,z}} \\ \vdots & \frac{\partial U}{\partial q_{i,w}} & \vdots \\ \frac{\partial U}{\partial q_{n,x}} & \frac{\partial U}{\partial q_{n,y}} & \frac{\partial U}{\partial q_{n,z}} \end{bmatrix} = \begin{bmatrix} \vec{\mathcal{F}}_0 \\ \vdots \\ \vec{\mathcal{F}}_i \\ \vdots \\ \vec{\mathcal{F}}_n \end{bmatrix} \quad (2.15)$$

106 where  $\frac{\partial}{\partial q_{i,w}}$  is the derivative with respect to  $q$  where  $w$  denotes direction of the deriva-  
 107 tive ( $x$ ,  $y$ , or  $z$ ),  $n$  is the number of atoms and  $U$  is the potential which depends on  
 108  $q$ , and  $\vec{F}_i$  is the "force" on the  $i$ th atom.

109 **No-U-Turn-Sampling**

110 **Grand Canonical Ensemble**

111 **Ensemble description**

112 In the Grand Canonical Ensemble (GCE) two sets of variables are allowed to change,  
 113 the atomic positions and the total number of atoms and their associated identities.  
 114 These two variables are controlled by temperature and chemical potential. The par-  
 115 tition function is

$$\Xi = e^{-\beta(\mathcal{H}+\mu)} \quad (2.16)$$

116 This is translated into a Monte Carlo system, producing Grand Canonical Monte  
 117 Carlo (GCMC).

118 **Grand Canonical Monte Carlo**

119 While the probabilities for atomic motion are the same as in the Canonical Ensemble,  
 120 the addition or removal of an atom have their own probabilities. For the addition of  
 121 an atom the probability is formally:

$$\min[1, \frac{V}{(N+1)\Lambda(T)^3} e^{-\beta\Delta U + \beta\mu}] \quad (2.17)$$

122 Similarly the removal of an atom has the probability:

$$\min[1, \frac{(N)\Lambda(T)^3}{V} e^{-\beta\Delta U - \beta\mu}] \quad (2.18)$$

123 However, both of these equations depend of the overall simulation volume and the  
 124 thermal wavelength, which is undesirable as these are not really properties that we

125 are of interest to these simulations. Thus, we roll them into the definition of the  
126 chemical potential, essentially setting the base chemical potential to counteract these  
127 effects. This makes certain that our simulation does not change if we change the  
128 overall cell volume. A GCMC move consists of creating a new atomic configuration,  
129 where an atom has been added or removed, and checking the above criteria. However,  
130 previous results have shown that this method is computationally expensive in dense  
131 liquids, and exceedingly expensive in solid materials. The long simulation times  
132 are due to the random nature of the atomic additions or removals which produce:  
133 over-tightly packed atoms, atoms in the middle of nowhere, or unphysical vacancies.  
134 These configurations are rejected by the GCMC criteria but their probability of being  
135 sampled is much higher than configurations which are lower in energy, since the  
136 number of incorrect ways to add/remove atoms is much larger than the correct ways.  
137 Thus we have implemented methods for biasing the atomic addition positions and  
138 the atomic removals toward configurations which are more likely to be accepted.

### 139 GCMC biasing

140 The first method is to remove some of the excess options from the probability pool.  
141 Initially the insertion positions are calculated at random using a random number gen-  
142 erator and scaled to the size of the simulation cell. This produces probabilities which  
143 have floating point level precision, which is effectively infinite. While this produces  
144 a potentially infinite number of ways to create energetically favorable configurations,  
145 the infinite ways to produce bad configurations is much larger. Thus we can limit this  
146 by moving to voxels. In this case atoms are added to the center of voxels which have  
147 a pre-set resolution, limiting our total number of valid addition points. While this  
148 could produce some problems with ergodicity, we avoid this by allowing the atoms to  
149 translate throughout the system. Each voxel has a probability of being tried:

$$P_{i,j,k} = \frac{xyz}{abc} \quad (2.19)$$

150 where  $x, y, z$  and  $a, b, c$  are the resolutions and cell side lengths in the cardinal di-  
151 rections, respectively. While this does help to limit the total probability space it  
152 does not tell us which voxels are likely to lead to better configurations, leading to  
153 many rejected atomic additions. To combat this issue we can weigh the individual  
154 voxels, giving more probability to voxels which show promise and less to those with  
155 less likelihood to be accepted.

156 The approach most likely to yield success would be to measure the change in  
157 potential energy associated with the addition of an atom at the center of the voxel  
158 where the probability of a voxel to be tried is:

$$P_{i,j,k} = \frac{e^{\beta\Delta U_{i,j,k}}}{\sum_{i,j,k} e^{\beta\Delta U_{i,j,k}}} \quad (2.20)$$

159 where  $\Delta U_{i,j,k}$  is the change in energy. However, calculating  $\Delta U_{i,j,k}$  can be particu-  
160 larly expensive, especially when calculating scattering from atomic positions. The  
161 computational expense can be mitigated by using a cheaper potential, if only for the  
162 evaluation of the voxel energy, as previously shown. Similar to previous work we can  
163 use the Lennard Jones potential to approximate the addition potential.

164

## CHAPTER 3

165

### ATOMIC PAIR DISTRIBUTION FUNCTION:

166

### THEORY AND COMPUTATION

167 3.1 THEORY

168 To properly understand the PDF and its limitations we need to derive its mathemat-  
169 ics. The following derivation has been performed numerous times but most recently  
170 and completely by Farrow and Billinge, it is reproduced here for clarity and com-  
171 pleteness.

172 **Derivation**

173 **Analytical Gradients**

174 Many optimization algorithms and simulations methodologies, including HMC, re-  
175 quire not only the potential energy of a given configuration but also the forces acting  
176 on that configuration. These forces are described by the gradient of potential energy  
177 of the system which in turn requires the gradient of the PDF. As previously shown the  
178 PDF is the Fourier Transform of the Debye equation. Since the Fourier Transform is  
179 expressed as an integral we can exchange the order of the gradient and the integral,  
180 allowing us to calculate the analytical gradient of the Debye equation and FFT the  
181 resulting function. The Debye equation, with a Debye-Waller vibrational correction  
182 is

$$F(Q) = \frac{1}{N\langle f \rangle^2} \sum_{j \neq i} f_i^*(Q) f_j(Q) \exp(-\frac{1}{2}\sigma_{ij}^2 Q^2) \frac{\sin(Qr_{ij})}{r_{ij}} \quad (3.1)$$

183 where

$$\sigma_{ij}^2 = (\vec{u}_{ij} * \hat{d}_{ij})^2 \quad (3.2)$$

$$\vec{u}_{ij} = \vec{u}_i - \vec{u}_j \quad (3.3)$$

$$\hat{d}_{ij} = \frac{\vec{d}_{ij}}{r_{ij}} \quad (3.4)$$

$$r_{ij} = \|\vec{d}_{ij}\| \quad (3.5)$$

$$\vec{d}_{ij} = \begin{bmatrix} q_{ix} - q_{jx} \\ q_{iy} - q_{jy} \\ q_{iz} - q_{jz} \end{bmatrix} \quad (3.6)$$

184 where  $Q$  is the scatter vector,  $f_i$  is atomic scattering factor of the  $i$ th atom, and  $r_{ij}$   
 185 is the distance between atoms  $i$  and  $j$  and has  $q$  dependence. For simplicities sake  
 186 we will break up  $F(Q)$  so that

$$F(Q) = \alpha \sum_{j \neq i} \beta_{ij} \tau_{ij} \Omega_{ij} \quad (3.7)$$

187 where

$$\alpha = \frac{1}{N\langle f \rangle^2} \quad (3.8)$$

$$\beta_{ij} = f_i^*(Q) f_j(Q) \quad (3.9)$$

$$\tau_{ij} = \exp(-\frac{1}{2} \sigma_{ij}^2 Q^2) \quad (3.10)$$

$$\Omega_{ij} = \frac{\sin(Qr_{ij})}{r_{ij}} \quad (3.11)$$

188 The derivatives are as follows:

$$\frac{\partial}{\partial q_{i,w}} F(Q) = \alpha \sum_j \beta_{ij} \left( \frac{\partial \tau_{ij}}{\partial q_{i,w}} \Omega_{ij} + \tau_{ij} \frac{\partial \Omega_{ij}}{\partial q_{i,w}} \right) \quad (3.12)$$

189 where

$$\frac{\partial \Omega_{ij}}{\partial q_{i,w}} = \frac{Q \cos(Qr_{ij}) - \Omega_{ij}}{r_{ij}^2} (q_{i,w} - q_{j,w}) \quad (3.13)$$

$$\frac{\partial \tau_{ij}}{\partial q_{i,w}} = \frac{\sigma_{ij} Q^2 \tau_{ij}}{r_{ij}^3} ((q_{i,w} - q_{j,w}) \sigma_{ij} - (u_{i,w} - u_{j,w}) r_{ij}^2) \quad (3.14)$$

190 Since  $\vec{u}_{ij}$  is a variable as well, we need the derivative with respect to it as well.

191 Thus

$$\frac{\partial}{\partial u_{i,w}} F(Q) = \alpha \sum_j \beta_{ij} \frac{\partial \tau_{ij}}{\partial u_{i,w}} \Omega_{ij} \quad (3.15)$$

$$\frac{\partial \tau_{ij}}{\partial u_{i,w}} = -\frac{\sigma_{ij} Q^2 \tau_{ij}}{r_{ij}} (q_{i,w} - q_{j,w}) \quad (3.16)$$

## 192 Without ADPs

193 Without ADPs the equations simplify down to

$$F(Q) = \frac{1}{N \langle f \rangle^2} \sum_{j \neq i} f_i^*(Q) f_j(Q) \frac{\sin(Qr_{ij})}{r_{ij}} \quad (3.17)$$

194 and

$$\frac{\partial}{\partial q_{i,w}} F(Q) = \alpha \sum_j \beta_{ij} \frac{\partial \Omega_{ij}}{\partial q_{i,w}} \quad (3.18)$$

195 use of these equations, when ADPs are not appropriate (like at cryogenic tempera-  
196 tures), greatly speeds up the computaiton.

## 197 3.2 COMPUTATION

198 Simply deriving the equations for the PDF is not enough. The many body nature of  
199 the PDF equation make analytical solution of the structure from the PDF impossible.  
200 Thus, the PDF must be computed from a structural candidates and compared against  
201 experimental results to evaluate the reliability of the model.

## 202 HPC and GPUs

203 To properly solve the structure of materials the PDF will need to be computed many  
204 times and checked against experimental results. This requires computation of the  
205 PDF, potentialy over many atoms. Calculating these PDFs requires a fast, highly  
206 parallized, computational framework.

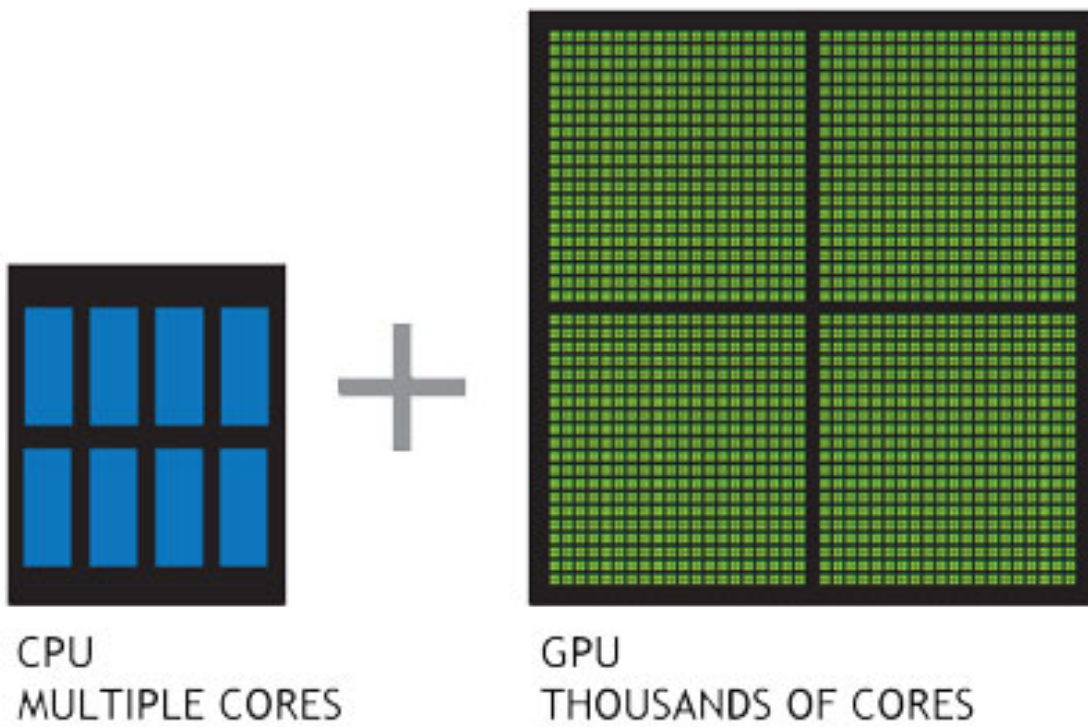


Figure 3.1: Comparison of the CPU and GPU chip architectures

### 207    GPUs and Parallelization

208    Computing the PDF is an embarrassingly parallel problem. The basic procedure is  
 209    to calculate the reduced structure factor  $F(Q)$  for each atom pair and momentum  
 210    transfer vector, sum over all the atom pairs, and Fourier transform the structure to  
 211    the PDF. The first part of this procedure is perfectly parallelizable, as each atom pair is  
 212    separate from the others. The summation over all the atomic reduced structure factors  
 213    can be parallelized via distributed summing. Lastly the FFT can be parallelized using  
 214    existing parallel FFT algorithms.

215    GPUs are particularly well suited to the task of computing PDFs. GPU chip  
 216    architecture is designed to perform many tasks simultaneously by having potentially  
 217    thousands of cores.

218 Map from  $ij$  space to  $k$  space

219 The above equations, although formally correct, are very ineffiecent.  $F(Q)$  and its  
 220 gradient are indexed over all the atoms twice, however there are symmetries that  
 221 allow us to only compute over the atom pairs esentially mapping from an  $n \times n$  space,  
 222  $ij$  space, to a  $\frac{n(n-1)}{2}$  space,  $k$  space. For  $F(Q)$  we apply the following mapping where

$$\begin{array}{ccccc} & & \psi & & \\ E & \xrightarrow{\quad} & E' & \xrightarrow{\Sigma} & Z \\ \phi \downarrow & & & \nearrow \Sigma' & \\ B & \xrightarrow{\quad} & B' & & \end{array}$$

223

224  $E$  denotes the atomic coordinates in  $ij$  space,  $E'$  denotes  $F(Q)$  before the summation  
 225 in  $ij$  space,  $B$  denotes the atomic pairs in  $k$  space,  $B'$  denotes  $F(Q)$  in  $k$  space, and  
 226  $Z$  denotes the final summed  $F(Q)$ . For the operators,  $\phi$  denotes the mapping from  
 227  $ij$  space to  $k$  space  $k = j + i * \frac{i-1}{2}$ ,  $\psi$  and  $\psi'$  denote the  $F(Q)$  operation in  $ij$  and  $k$   
 space, respectivly.  $\Sigma$  denotes the sum over all the atoms.

228 To properly define  $\Sigma'$  we must establish whether  $F(Q)$  is an even function. We  
 229 can accomplish this by examining each of the portions of  $F(Q)$ ,  $\alpha, \beta, \tau, \Omega$ .  $\Omega$  is even,  
 230 since  $r_{ij}$  is the interatomic distance, which is the same despite a flip of indicies,  $Q$   
 231 does not depend on the atomic indicies, and since  $Qr_{ij}$  is even so is  $\sin Qr_{ij}$ . Thus,  
 232  $\Omega$  is even. Providing similar analysis to  $\tau$  we can see that while  $\vec{u}_{ij}$  is odd, so is  
 233 the unit displacement vector between the two atoms, thus the two odds cancel out.  
 234 Intuitivly this makes sense, since the  $F(Q)$  equation is fundamentally interested in the  
 235 interatomic distances which is even. Thus, switching atom indicies does not change  
 236  $F(Q)$ . Due to the even nature of the  $F(Q)$  operator the  $\Sigma'$  operator sums over all the  
 237 atom pairs, and multiplies by two to reflect the double counting of the  $\Sigma$  operator.

238 For the gradient a similar mapping is used:

239 In this mapping, however, we use the  $\tilde{\phi}\Sigma$  operator. This operator simultaniously

$$\begin{array}{ccccc}
& & \psi & & \Sigma \\
E & \xrightarrow{\quad} & E' & \xrightarrow{\quad} & Z \\
\phi \downarrow & & & \nearrow \tilde{\phi}\Sigma & \\
B & \xrightarrow{\quad} & B' & & 
\end{array}$$

240 performs a reverse mapping from  $k$  to  $ij$  space, and a summation with the correct  
 241 symmetry. In this case the  $\psi$  and  $\psi'$  operators, which denote the  $\vec{\nabla}F(Q)$  operator  
 242 in  $ij$  and  $k$  space, are antisymmetric. Intuitivly this makes sense as an extension of  
 243 Newton's Second Law, since each particle's interation is felt oppositely by its partner.

#### 244 Periodic Boundary Conditions

245 Periodic boundary conditions can be helpful when simulating extended solids or large  
 246 nanoparticles. In this case all the non-crystallinity is contained within the simulation  
 247 box and the box is repeated to create the longer distance peaks observed in the PDF.  
 248 To perform this we can break up the Debye equation into two main parts, the part  
 249 that describes the interatomic distances within the simulation box and those between  
 250 boxes. Neglecting the thermal motion portion:

$$F(Q) = \frac{1}{N\langle f \rangle^2} \left( \sum_{j \neq i} f_i^*(Q) f_j(Q) \frac{\sin(Qr_{ij})}{r_{ij}} + \sum_{i,j} f_i^*(Q) f_j(Q) \frac{\sin(QR_{ij})}{R_{ij}} \right) \quad (3.19)$$

251 where

$$R = |\vec{r} + \vec{u}| \quad (3.20)$$

$$\vec{u} = \gamma_1 * \vec{a} + \gamma_2 * \vec{b} + \gamma_3 * \vec{c} \quad (3.21)$$

#### 252 3.3 EXPERIMENT

253 PDF experiments are generally performed at synchrotron light sources, as only these  
 254 sources can provide the need flux, energy, and high momentum transfer vectors needed  
 255 to obtain relyable PDFs.

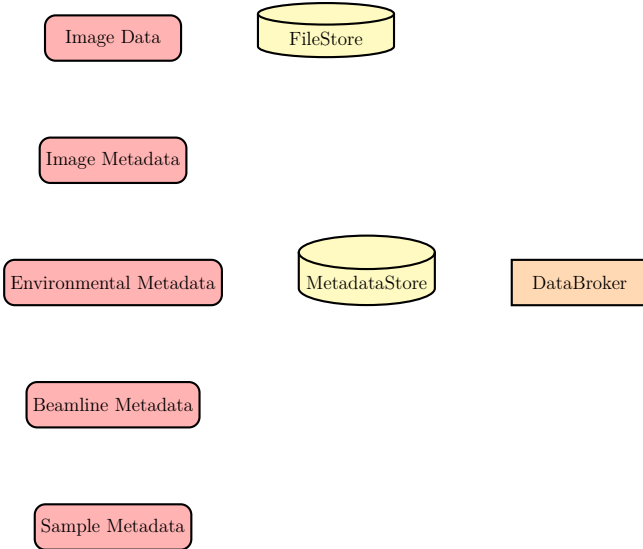


Figure 3.2: Database Loading Workflow. Data is loaded from various sources, including images and text files, into the FileStore and MetadataStore databases. Data is then retrieved from the databases using the databroker.

256 3.4 DATA PROCESSING WORKFLOW

257 Processing the raw pixel intensities to the PDF is very important as we are extracting  
 258 most of our interesting information out of very high  $Q$  data. This data relies on good  
 259 statistics and sound background subtraction. Talk about papers from Billinge Group  
 260 with thin film PDF and dilute NP solutions. Diagram of the overall data processing  
 261 workflow. Discuss the NSLS-II data stack.

262 **MetadataStore Side Loading**

263 Design of sidewinder-spec for loading the data into metadatastore. Most of the design  
 264 considerations went into the loaders, which are different for each experiment.

265 **Detector  $Q$  resolution**

266 To properly azimuthally integrate the images taken from the detector the  $Q$  resolution  
 267 of the pixels must be calculated. Integrating using even bins will cause pixels which

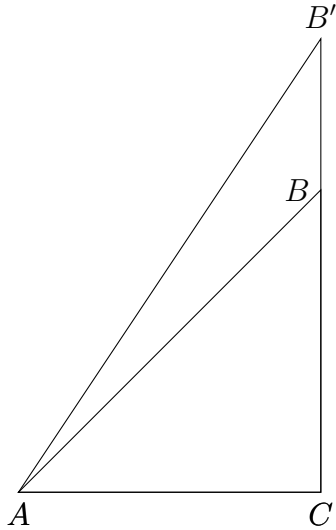


Figure 3.3: Scattering onto a flat detector

268 are not on the same ring to be binned together, causing the incorrect value of  $I(Q)$   
 269 to be obtained and a larger standard deviation in the integrated data. To properly  
 270 calculate the  $Q$  resolution the resolution of each of the pixels in  $2\theta$  must be calculated.  
 271 Figure 3.3 shows the scattering of x-rays onto a flat image plate detector. In this  
 272 diagram the bottom of the  $n$ th pixel is  $B$  while the top is  $B'$ . The resolution of this  
 273 pixel in  $2\theta$  is  $\angle BAC - \angle B'AC$ . Thus the resolution, calculated from the distances is

$$\Delta 2\theta = \arctan \frac{b}{d} - \arctan \frac{t}{d} \quad (3.22)$$

274 where  $d$  is the sample to detector distance,  $b$  is the distance to the bottom of a pixel,  
 275 and  $t$  is the distance to the top of that pixel. Note that these distances need to have  
 276 been corrected for detector tilt and rotation. Thus the resolution of a pixel in  $Q$  is

$$\Delta Q = \frac{4\pi(\sin \arctan \frac{b}{d} - \sin \arctan \frac{t}{d})}{\lambda} \quad (3.23)$$

277 where  $\lambda$  is the x-ray wavelength.

278 For a Perkin Elmer image plate, like the one used at the NSLS-II's XPD and the  
 279 APS's 11-ID-B, the resolution function is shown in 3.4. For the same detector the  
 280 number of pixels per  $Q$  is shown in 3.5

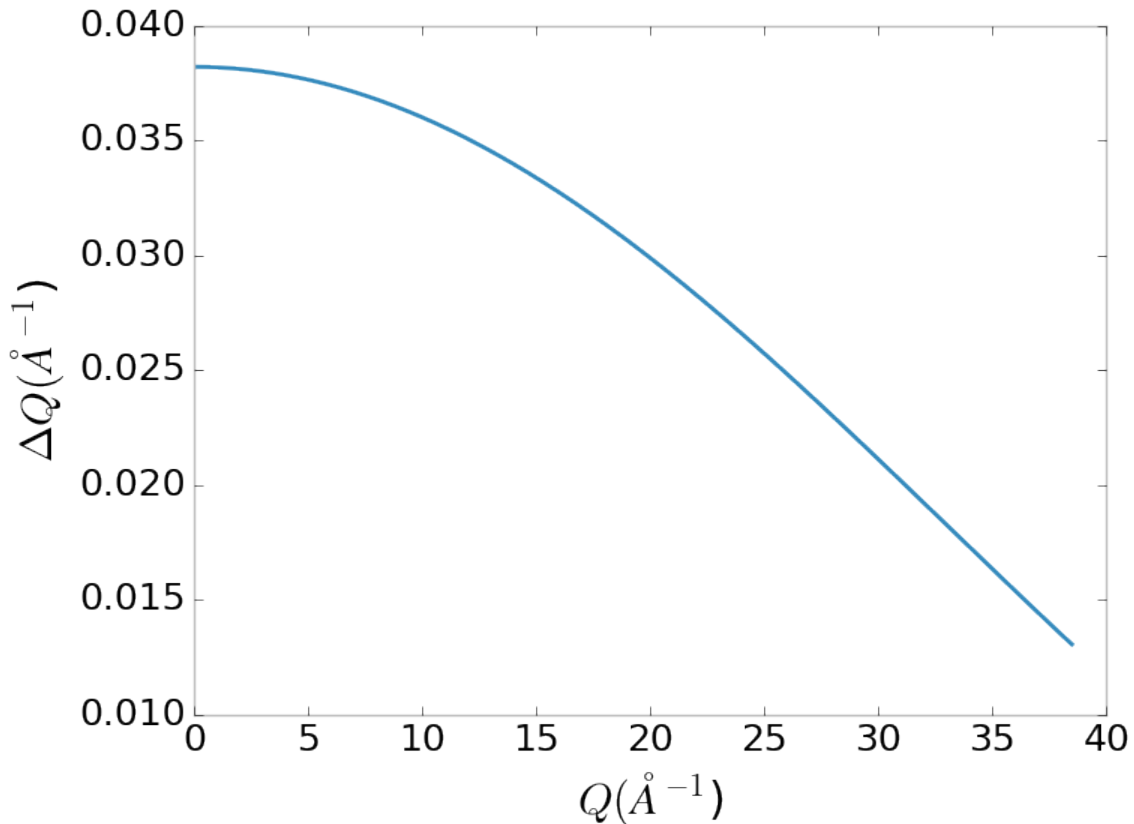


Figure 3.4:  $Q$  resolution as a function of  $Q$ .

## 281 Automated Mask Generation

### 282 Introduction

283 Detector masking is an important part of any x-ray scattering workflow as dead/hot  
284 pixels, streak errors, and beamstop associated features can be averaged into the data  
285 changing the signal and its statistical significance. While some features, like the  
286 beamstop holder, can be easily observed and masked by hand other are much more  
287 difficult to observe even on large computer monitors. Additionally, while dead/hot  
288 pixels and streaks are usually static the hot pixels associated with textured or sin-  
289 gle crystal scattering or cosmic rays are not. Thus, coming up with an automated  
290 method for finding such erroneous pixels is important, especially as high flux diffrac-  
291 tion beamlines can generate data very quickly.

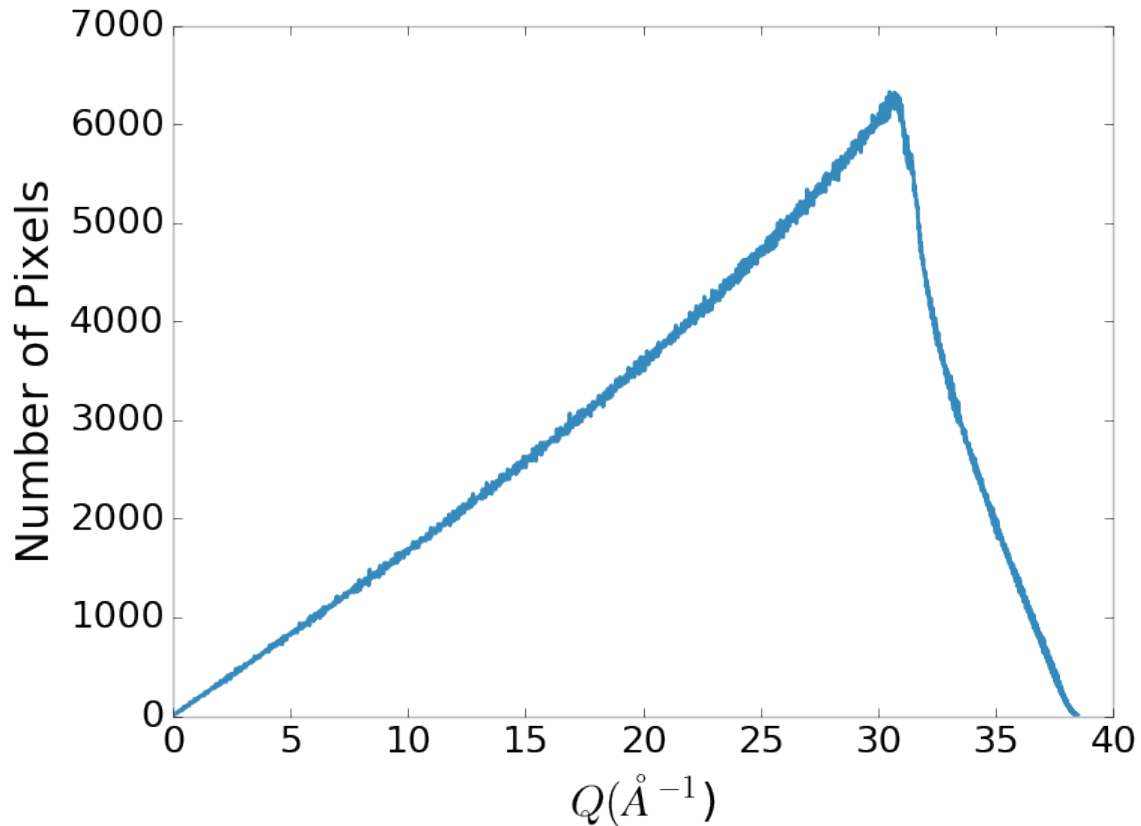


Figure 3.5: Number of pixels as a function of  $Q$ , binned at the  $Q$  resolution of the detector.

292 While this problem can be quite complex in the most general case, we can use the  
 293 annular symmetry of the powder scattering pattern to our advantage, by comparing  
 294 a pixel against pixels in the same ring. Since non-textured powder scattering should  
 295 produce the same pixel intensity for a given ring we can mask any pixels which are  $\alpha$   
 296 standard deviations away from the mean. This method relies on the aforementioned  
 297 pixel binning algorithm, as using miss sized bins will cause some pixels which should  
 298 be in separate rings to be put together, and others which should be in the same ring  
 299 to be separated. In that case the masking algorithm will overestimate the number of  
 300 pixels to be masked due to the additional statistical variation in the sample.

301 **Algorithm Design**

302 The masking algorithm procedure takes in the image and a description of the pixel  
303 positions in either distance from the point of incidence or in  $Q$ . The image is then  
304 integrated twice, producing both the mean  $I(Q)$  and the standard deviation of each  
305  $I(Q)$  ring. The mask is created by comparing the pixel values against each ring's  
306 standard deviation and threshold  $\alpha$ . Note that the threshold can be a function of  
307 distance from the point of incidence or  $Q$ .

308 **Test Cases**

309 To study the effectiveness of the masking we ran the algorithm against both simulated  
310 experimental data. In the case of the simulated data four systems were created: 1)  
311 dead/hot pixels with varying numbers of defective pixels, 2) beamstop holder with  
312 varying beamstop holder transmittance, 3) rotated beamstop holder with varying  
313 beamstop holder transmittance, and 4) beamstop holder with dead/hot pixels. The  
314 base scattering was produced by

$$I = 100 \cos(50r)^2 + 150 \quad (3.24)$$

315 where  $r$  is a pixel's distance from the beam point of incidence. The positions of  
316 the dead/hot pixels were chosen at random as was the dead or hot nature of the  
317 defect. Dead pixels had values from 0 to 10, while hot pixels had values from 200  
318 to 255. The beamstop was positioned at the vertical center of the detector with an  
319 initial width of 60 pixels and final width of 120 pixels. The height of the beamstop  
320 was 1024 pixels. The beamstop was calculated to attenuate the x-ray scattering  
321 signal at various transmittance, as various beamstop holder materials have different  
322 transmittance. Two versions of the masking algorithm were run for each test case, one  
323 using the standard even bin sizes for the integration step, and one where the bin sizes  
324 are tuned to the pixel  $Q$  resolution as discussed in 3.4.

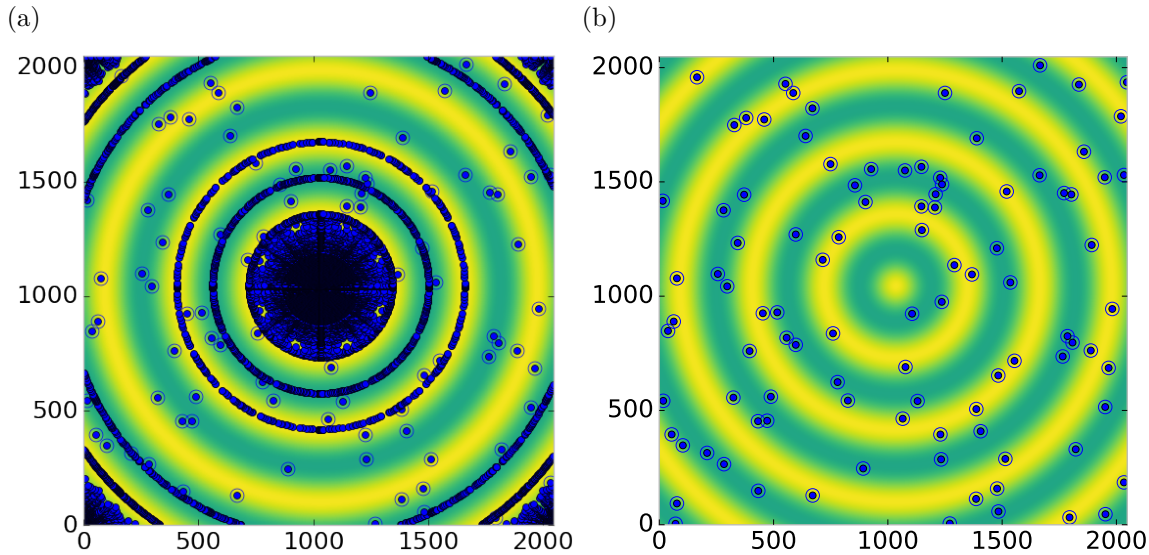


Figure 3.6: Generated dead/hot pixel masks for a detector with 100 bad pixels. a) the standard even bin mask and b) the  $Q$  resolution binned mask

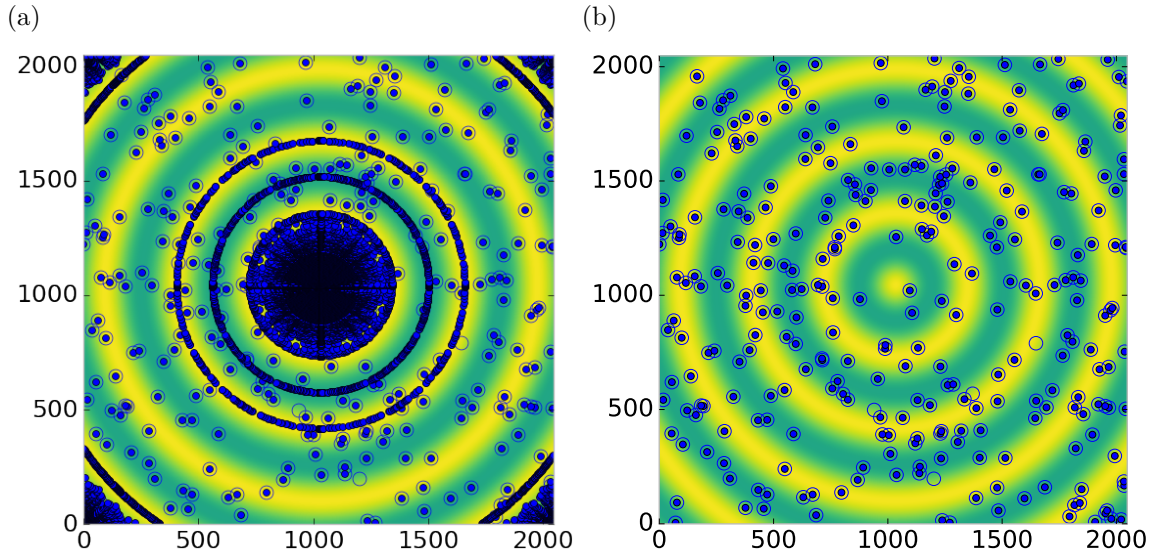


Figure 3.7: Generated dead/hot pixel masks for a detector with 300 bad pixels. a) the standard even bin mask and b) the  $Q$  resolution binned mask

### 325 Results and Discussion

326 Figures 3.6-3.13 show the results of the masking algorithm on simulated images. The  
 327 dead/hot pixel masking shows the importance of using the  $Q$  resolution based bin sizes

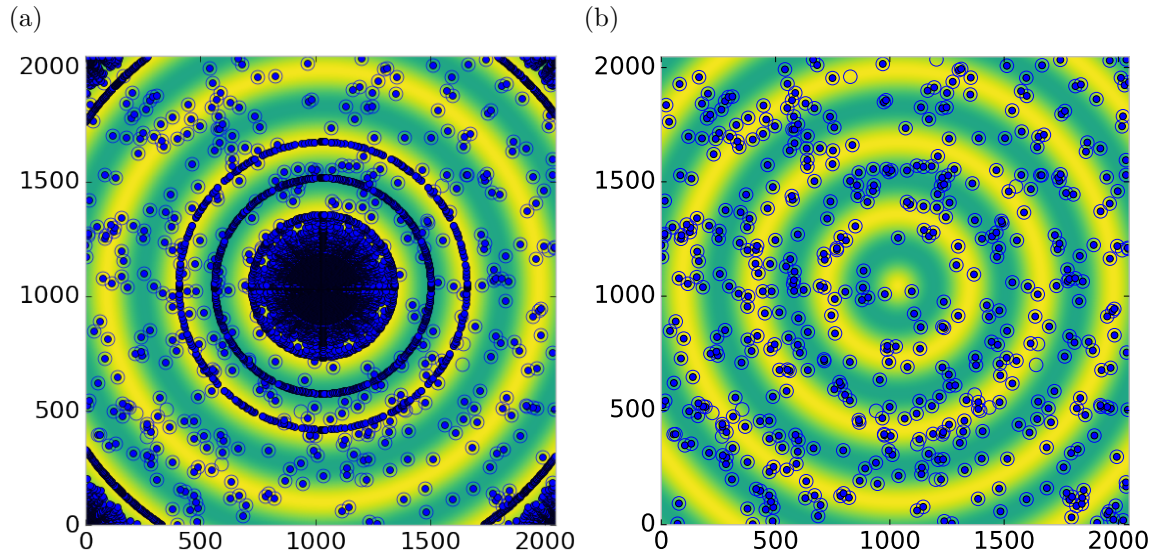


Figure 3.8: Generated dead/hot pixel masks for a detector with 500 bad pixels. a) the standard even bin mask and b) the  $Q$  resolution binned mask

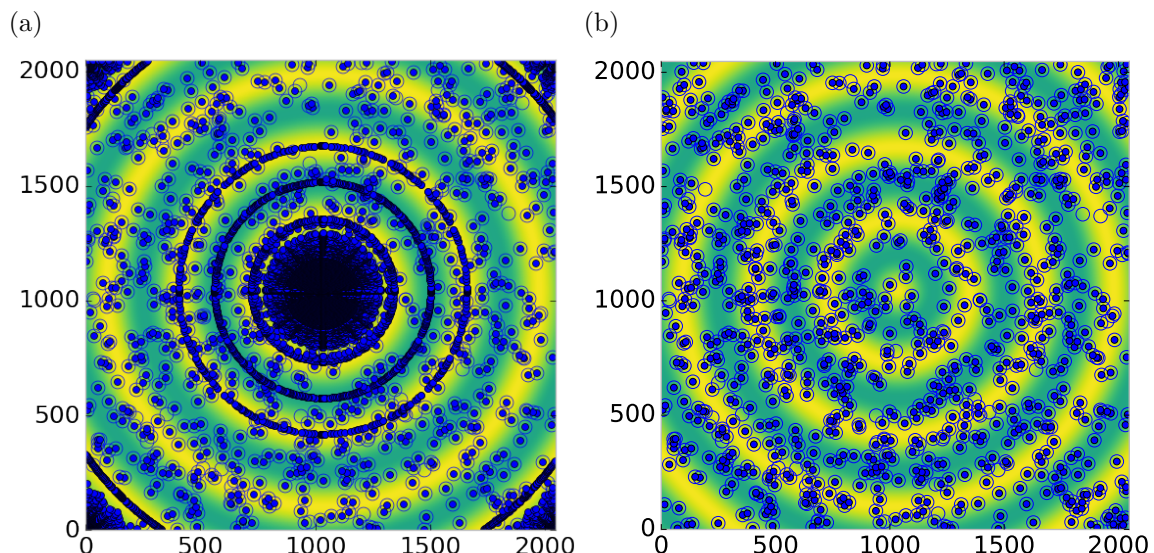


Figure 3.9: Generated dead/hot pixel masks for a detector with 1000 bad pixels. a) the standard even bin mask and b) the  $Q$  resolution binned mask

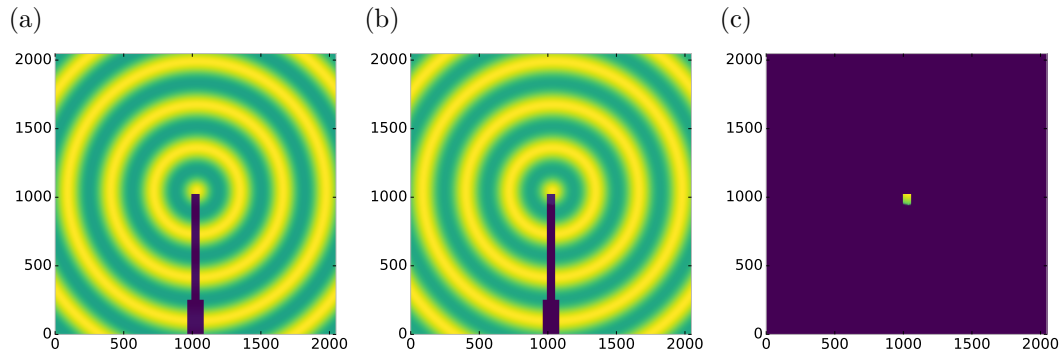


Figure 3.10: Generated beamstop holder masks for a beamstop holder with 10% transmittance. a) the raw image, b) the masked image, c) and the missed pixels

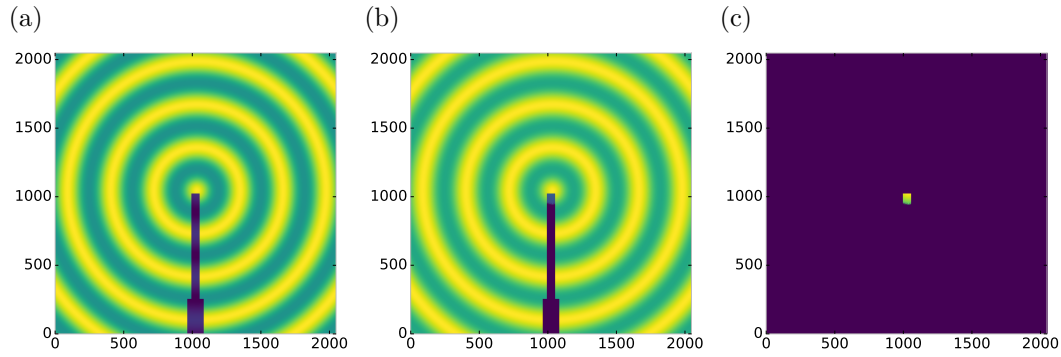


Figure 3.11: Generated beamstop holder masks for a beamstop holder with 30% transmittance. a) the raw image, b) the masked image, c) and the missed pixels

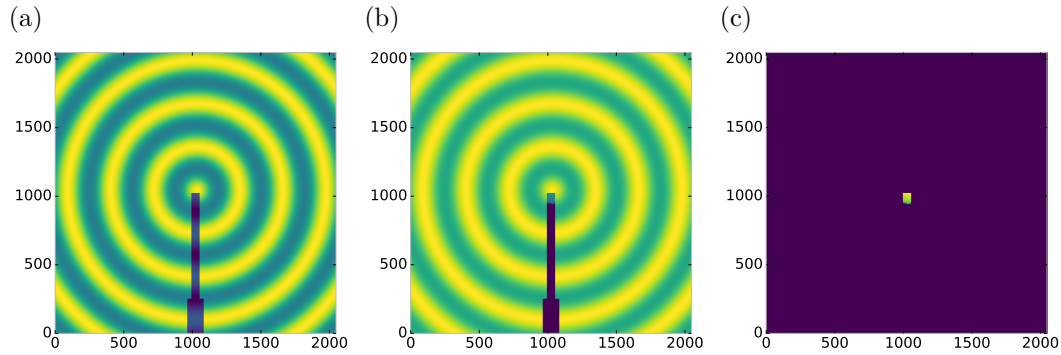


Figure 3.12: Generated beamstop holder masks for a beamstop holder with 50% transmittance. a) the raw image, b) the masked image, c) and the missed pixels

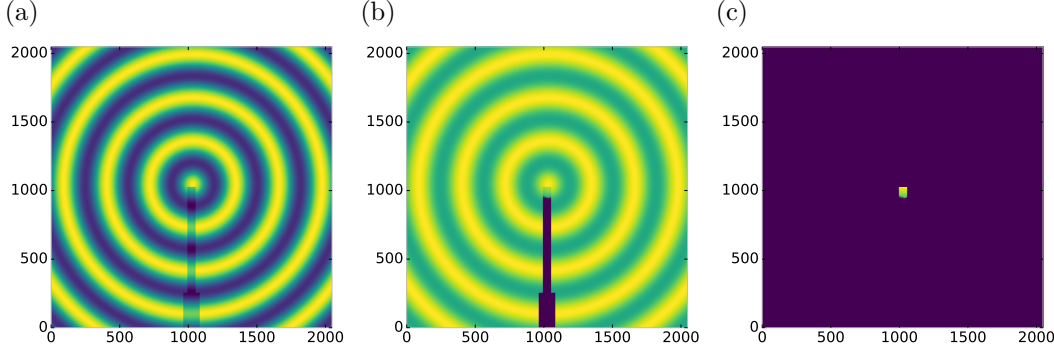


Figure 3.13: Generated beamstop holder masks for a beamstop holder with 90% transmittance. a) the raw image, b) the masked image, c) and the missed pixels

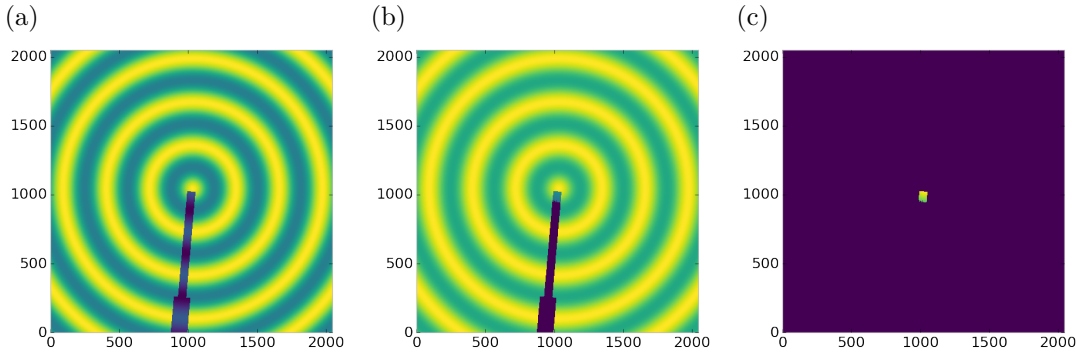


Figure 3.14: Generated beamstop holder masks which is rotated away from verticle

as the even bin based mask have a tendency to over mask the image, removing pixels which contain valuable signal. This overmasking is caused by pixels being improperly associated with one another by the even bins. Figure 3.6 indicates that the masking algorithm, with the proper binning, masks the image perfectly, with no missed bad pixels or good pixels masked. This is not the case in figures 3.7 - 3.9 as we can see pixels which should have been masked but were not. Despite these missed pixels no pixels were improperly masked in any of the well binned images. These test cases are actually more difficult than experimental data, as the dynamic range of most detector causes the dead/hot pixels and single crystal/texture peaks to be orders of magnitude away from the desired signal.

The beamstop holder masks shown in figures 3.10 - 3.13, which were all run with the  $Q$  resolution binning show similar results across the transmittance range, missing

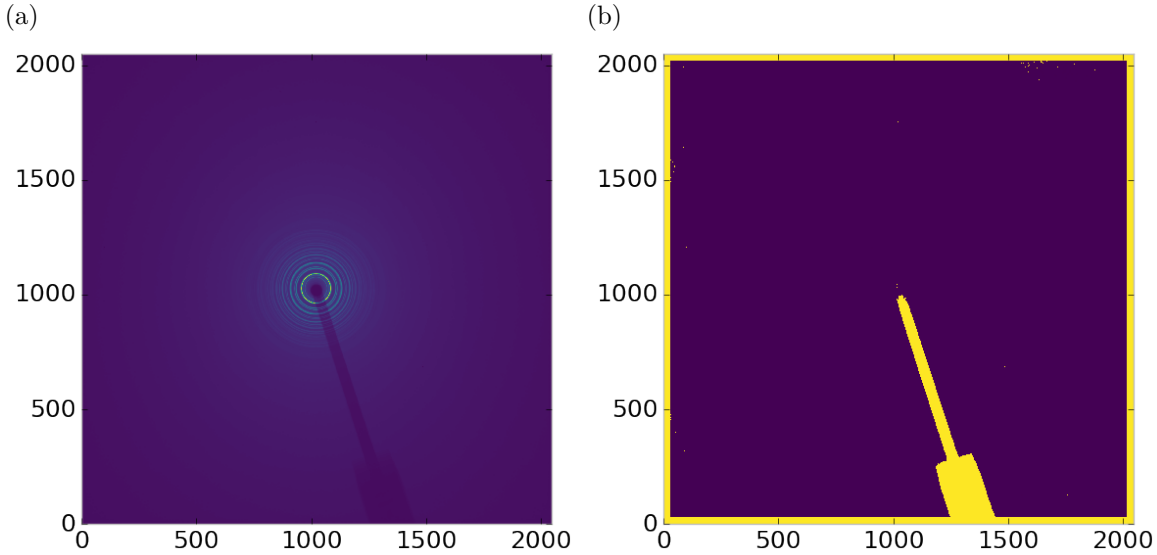


Figure 3.15: Masked experimental data. a) the raw image, b) the mask

only a small part of the beamstop holder near the point of incidence. Near this point the beamstop holder becomes a statistically significant part of the total number of pixels in a given ring, thus it can not be masked out using a statistical search of the rings. For most PDF and XRD studies this small area can be masked automatically by masking all the pixels who's distance from the point of incidence is smaller than a given radius  $r$ , or can be negelected outright as the area is not used in the analysis or refinement. Similar results were produced for beamstop holders which were rotated away from the vericle position, as shown in figure 3.14

Working with actual experimental data, obtained at the Advanced Photon Source beamline 11-ID-B, shows the difficulty of masking images which have low phonon counts. While the masking of experimental data taken with longer exposures, consisting of 250 .2 second shots, shown in figure 3.15 provides very sharp edges to the beamstop holder, and very little extra masking beyond the occasional dead pixel, this is not the case for the single crystal data. The single crystal data is more problematic because of its short exposure time and low flux, with 500 frame at a .1 second exposure and having shrunk the beam size. The low flux is to prevent the very strong

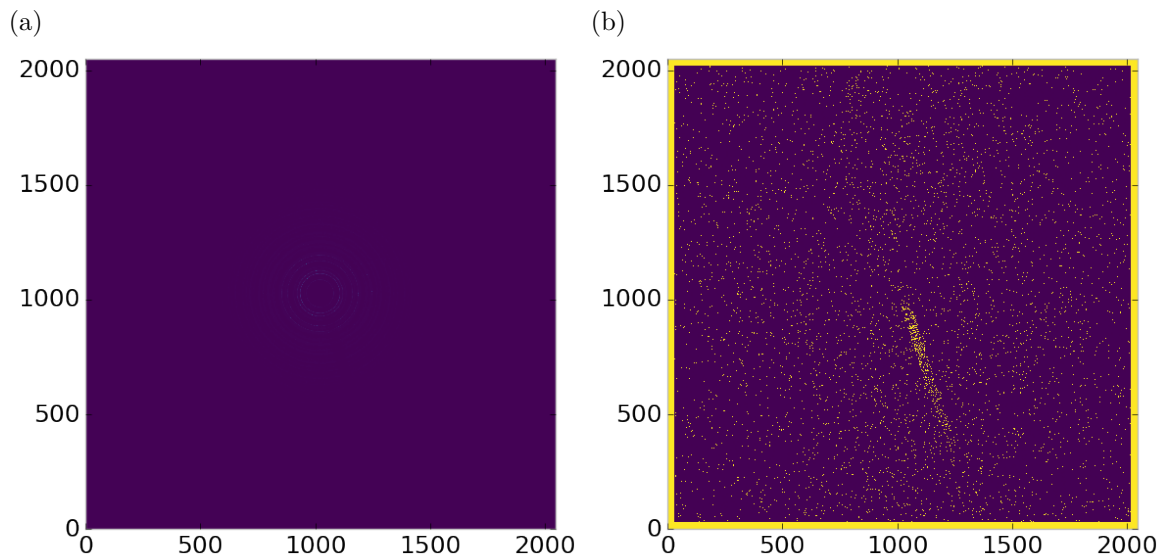


Figure 3.16: Masked experimental data with Pt single crystal signal. a) the raw image, b) the mask

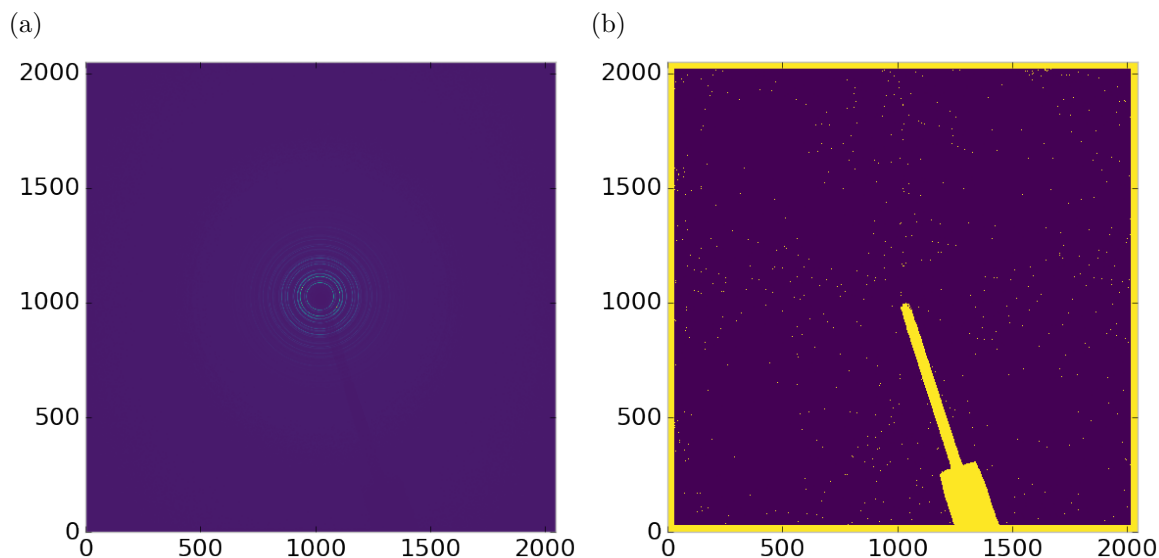


Figure 3.17: Masked experimental data with Pt single crystal signal using figure's 3.15 as a starting mask. a) the raw image, b) the mask

356 single crystal peaks from damaging the detector. However, this causes the image to  
357 be less statisticly viable then ideal, causing problems with the mask as seen in figure  
358 3.16. This can be aleviated to some degree by using the previously generated mask  
359 as a starting mask for the single crystal image, as shown in 3.17. While the masking  
360 algorithm still produces many diffuse masked pixels, they are far fewer, this may  
361 be due to the removal of the beamstop which could have contributed to the large  
362 standard deviation in figure 3.16.

### 363 **Conclusions**

364 In this section the masking algorithm, which relies on both  $Q$  resolution based binning  
365 and a statistical approach to azimuthal symmetry, was developed. The focus of  
366 this algorithm was to remove many unwanted detector features assocaited with pixel  
367 defect, beamstop holder associated scattering attenuation, and single crystal/texture  
368 peaks. Simulated data was used to evaluate the beamstop holder and dead/hot pixel  
369 masking capacity, while experimental data was used to check for single crystal and  
370 texture based masking.  $Q$  resolution based binning was shown to be very important to  
371 avoid overmasking. The ability of the mask writer to mask images is somewhat limited  
372 by the overall statistical image quality, although some deficiencies can be obtained by  
373 using previously generated masks as starting points. This masking algorithm is now  
374 in use in the data processing workflow and will be avaialable in scikit-beam soon.

### 375 **Automated Image Azimuthal Integration**

376 Using the  $Q$  resolution binning and masking developed in sections 3.4 and 3.4 the  
377 images can be properly integrated. Generally, images are integrated by taking the  
378 mean value of the pixels in a ring. However, other statistical measures of the average  
379 value can be used, like the median.

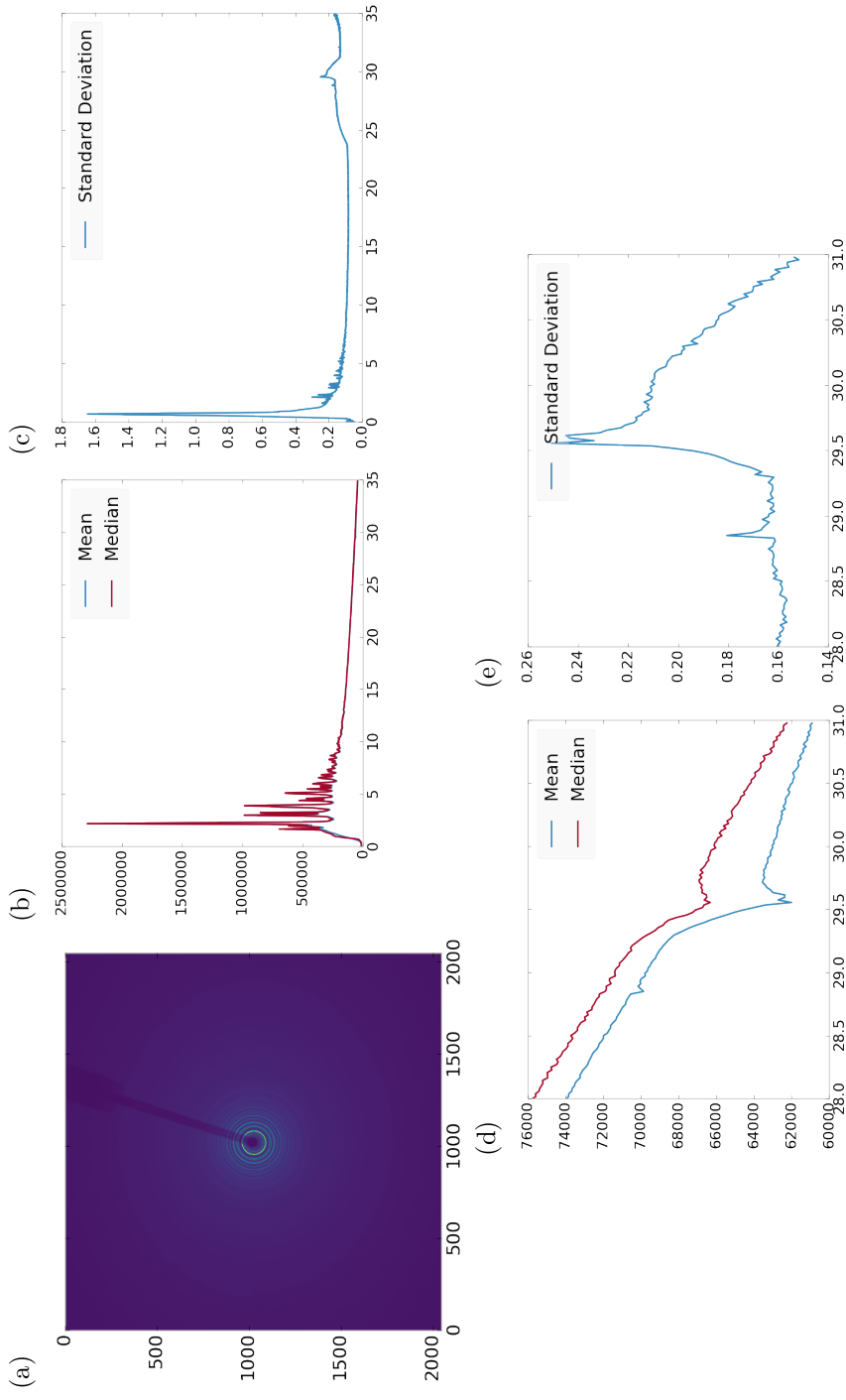


Figure 3.18: Masking, average, and % standard deviation of an example x-ray total scattering measurement. This image was produced with no mask. a) the image, b) the mean and median values, c) % standard deviation (normalized to the median), d) a closeup of the  $28 \text{\AA}^{-1}$  to  $31 \text{\AA}^{-1}$   $Q$  range for the mean and median, e)  $\text{\AA}^{-1}$  to  $31 \text{\AA}^{-1}$   $Q$  range for the standard deviation

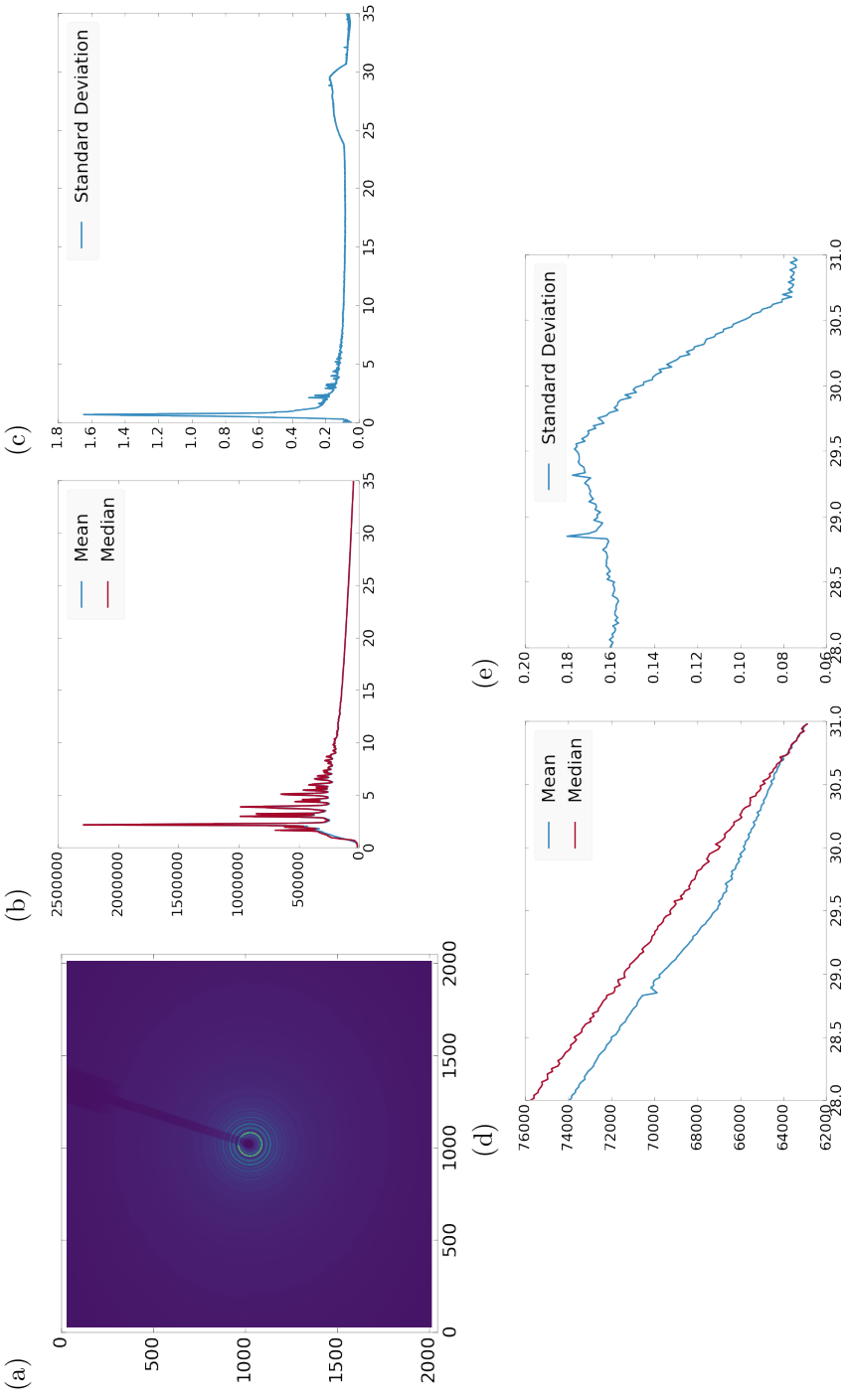


Figure 3.19: Masking, average, and % standard deviation of an example x-ray total scattering measurement. This image was produced with only an edge mask. a) the image, b) the mean and median values, c) % standard deviation (normalized to the median), d) a closeup of the 28 Å<sup>-1</sup> to 31 Å<sup>-1</sup>  $Q$  range for the mean and median, e) Å<sup>-1</sup> to 31 Å<sup>-1</sup>  $Q$  range for the standard deviation

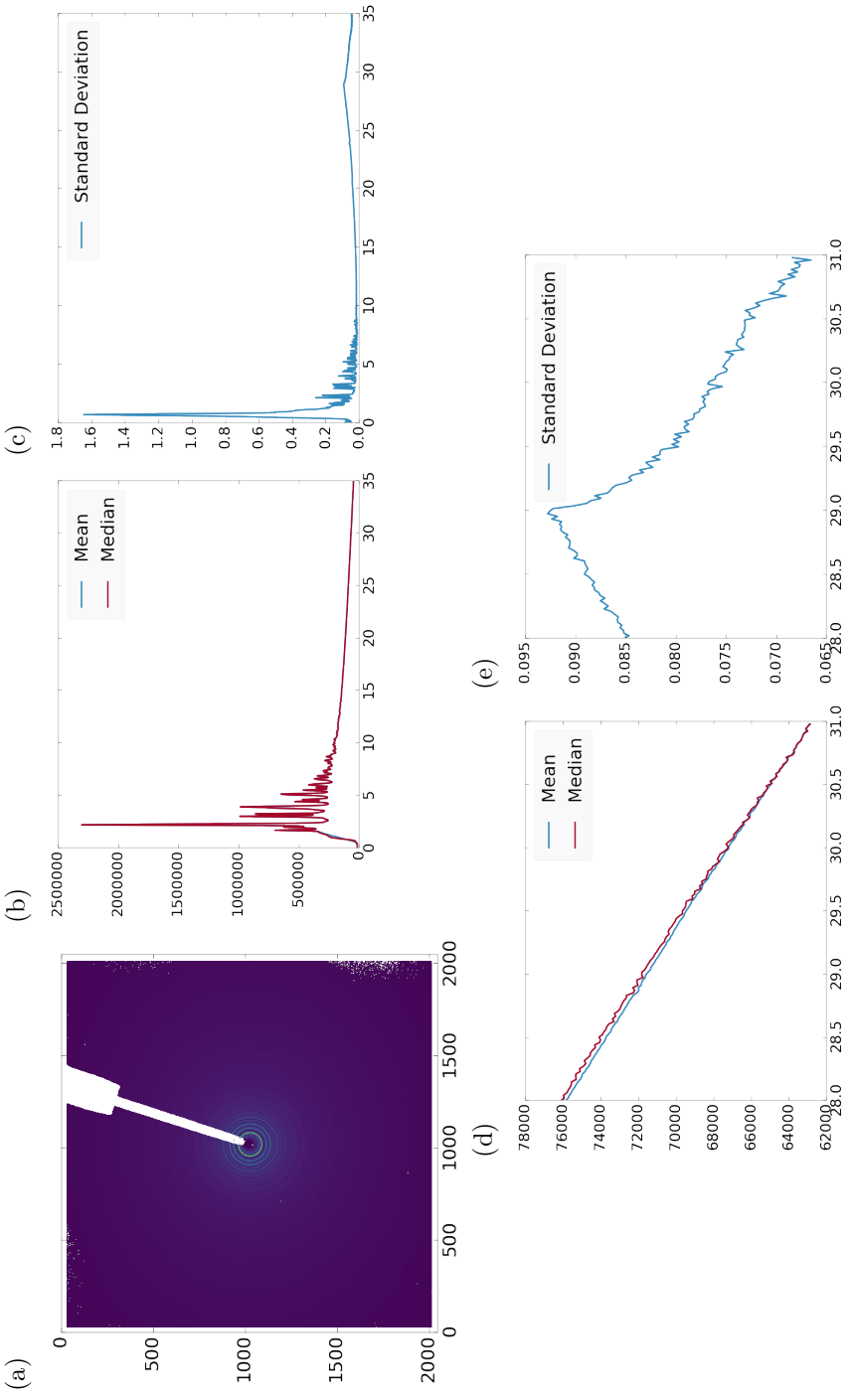


Figure 3.20: Masking, average, and % standard deviation of an example x-ray total scattering measurement. This image was produced combining an edge mask combined and the automatically generated mask. a) the image, b) the mean and median values, c) % standard deviation (normalized to the median), d) a closeup of the  $28 \text{ \AA}^{-1}$  to  $31 \text{ \AA}^{-1}$   $Q$  range for the mean and median, e)  $\text{\AA}^{-1}$  to  $31 \text{ \AA}^{-1}$   $Q$  range for the standard deviation

380

## CHAPTER 4

381

### BENCHMARKING

382 4.1 PDF

383 **Au55: surface relaxed**

384 **Au55: surface disordered**

385 **Au55: amorphous**

386 **Au102: triple phase**

387 **Au147**

388 **C60**

389 4.2 PDF WITH ADPs

390

## CHAPTER 5

391

### ANNEALING AND AGGREGATION OF 2NM

392

### AU NANOPARTICLES

393 5.1 EXPERIMENTS

394 **NP Synthesis**

395 **X-ray Total Scattering Measurements**

396 5.2 DATA PROCESSING

397 5.3 DATA ANALYSIS

398 5.4 SIMULATION

399 5.5 STRUCTURAL ANALYSIS

400 5.6 CONCLUSIONS

401

## CHAPTER 6

402

### PHASE CHANGES AND ANNEALING DYNAMICS OF

403

### $\text{Pr}_2\text{NiO}_4$ AND ITS DERIVATIVES

404 6.1 EXPERIMENTS

405  **$\text{Pr}_2\text{NiO}_4$  Synthesis**

406 **X-ray Total Scattering Measurements**

407 6.2 DATA PROCESSING

408 6.3 DATA ANALYSIS

409 **Intra Sample Comparison**

410 **Inter Sample Comparison**

411 6.4 SIMULATION

412 **Small Box**

413 **Large Box**

414 6.5 STRUCTURAL ANALYSIS

415 6.6 CONCLUSIONS

416

## CHAPTER 7

417

## CONCLUSION